JGR Solid Earth

RESEARCH ARTICLE
10.1029/2020JB021099

Stagnant Slabs and Their Return Flows From Finite-Frequency Tomography of the 410-km and 660-km Discontinuities

Zhen Guo[1,2] **and Ying Zhou**[1]

[1]Department of Geosciences, Virginia Tech, Blacksburg, VA, USA, [2]School of Science, Jiangnan University, Wuxi, Jiangsu, China

Key Points:

- The 410 and the 660 are deeper in major subduction zones with stagnant slabs
- Warm return flows associated with sinking slabs explain the mantle transition zone seismic structure
- Mass exchange between the upper and lower mantle occurs in the vicinity of the slabs

Supporting Information:

Supporting Information may be found in the online version of this article.

Correspondence to:

Y. Zhou,
yingz@vt.edu

Citation:

Guo, Z., & Zhou, Y. (2021). Stagnant slabs and their return flows from finite-frequency tomography of the 410-km and 660-km discontinuities. *Journal of Geophysical Research: Solid Earth*, *126*, e2020JB021099. https://doi.org/10.1029/2020JB021099

Received 30 SEP 2020
Accepted 10 APR 2021

Abstract Slab pull is generally considered as the dominant force that drives the global movement of tectonic plates. This convection mode is well constrained in the upper mantle but the convection pattern in the mid mantle is more speculative. In this study, we present high-resolution global models of the 410-km and 660-km discontinuity structure from finite-frequency tomography of SS precursors. The new models reveal a strong positive correlation between the two discontinuities under major subduction zones. In regions where large-scale stagnant slabs have been reported in the mantle transition zone (MTZ), both discontinuities occur at depths greater than the global average. This structure correlates well with seismic wavespeed anomalies, suggesting possible return flows from the lower mantle warming up the shallow MTZ above the stagnant slabs. Using a simple model for stagnant slabs in geodynamical simulations, we show that this mode of mass exchange between the upper mantle and the lower mantle occurs predominantly in the vicinity of the slabs, and, the return flows become stronger as the extent of slab stagnation increases.

1. Introduction

The movement of surface tectonic plates is generally considered to be driven by the pulling force associated with slab subduction (Forsyth & Uyeda, 1975). Upwellings at mid-ocean ridges are passive return flows in the shallow mantle in response to subduction at convergent plate boundaries. For example, seismic anomalies beneath the East Pacific Rise spreading centers are mostly confined in the uppermost 250 km (Webb & Forsyth, 1998). Subduction-driven convection has been well studied in the upper mantle while convective mass exchange in the mid mantle remains less clear. The mantle transition zone (MTZ) between the upper mantle and the lower mantle is bounded by two seismic discontinuities associated with pressure-induced mineral phase transitions, one from olivine to wadsleyite at about 410 km depth and a second one from ringwoodite to bridgmanite and ferropericlase at about 660 km depth (Anderson, 1967; Ringwood, 1969). The 660-km discontinuity is generally considered a possible barrier for whole mantle convection due to its negative Clapeyron slope (e.g., U. Christensen, 1995; Ringwood, 1994; Wada & King, 2015). In contrast, the Clapeyron slope of the 410-km discontinuity is positive. This predicts an anti-correlation between depth perturbations of the 410-km and the 660-km discontinuities for purely thermal anomalies in the MTZ (Bina & Helffrich, 1994; Katsura & Ito, 1989; Weidner & Wang, 2000).

In global seismic tomography, both penetrating and stagnant slabs have been imaged in the MTZ (Fukao & Obayashi, 2013; van der Hilst et al., 1997). However, structures in the MTZ are often not as well constrained as those in the upper or lower mantle. This is mainly because teleseismic body waves have turning depths in the lower mantle and fundamental-mode surface waves are only sensitive to wavespeed perturbations in the shallow mantle. Efforts have been made to utilize surface wave overtones to improve the resolution in the MTZ (e.g., Schaeffer & Lebedev, 2013). SS waves and their precursors S410S and S660S are waves reflected off the underside of the surface and the 410-km and the 660-km seismic interfaces, respectively. They provide constraints on depth perturbations of the two discontinuities and have been used to study the structure of the MTZ (Gu et al., 2003; Houser et al., 2008; Huang et al., 2019; Lawrence & Shearer, 2008; Shearer, 1991; Waszek et al., 2018; Yu et al., 2017). As secondary reflected waves, S410S and S660S waves (or SdS waves hereafter) are weak signals on recorded seismograms, and a common practice in global studies has been to stack their waveforms in a large circular area near their bounce points to improve signal-to-noise ratio

(Gu et al., 2003; Schmerr & Garnero, 2006; Shearer, 1991). While the effects of using different bin sizes in stacking have been investigated (Flanagan & Shearer, 1998; Houser et al., 2008), it is not surprising that discontinuity structures may not be well resolved because of large Fresnel zones associated with SS waves and their precursors (Lawrence & Shearer, 2008). The finite-frequency sensitivities of SS precursors have also been investigated based on adjoint calculations using the spectral element method (e.g., Koroni et al., 2017). When the length scale of discontinuity topography is comparable to the characteristic seismic wavelength, finite frequency effects become important.

In this study, we use a global data set of arrival time measurements of SS, S410S and S660S waves recorded at the Global Seismographic Network (GSN) to image depth perturbations of the 410-km and 660-km discontinuities at a global scale. We calculate finite-frequency sensitivities of arrival time measurements based on the Born approximation in the framework of traveling-wave mode coupling, which take into account complete wave interactions in every measurement window. In addition to accounting for wave diffractional effects in seismic tomography, the finite-frequency sensitivities allow us to identify measurements that are significantly contaminated by multiples of shallower interfaces or other seismic phases, in which case those measurements are excluded from imaging. This global data set allows us to obtain high resolution depth perturbations of the two discontinuities based on finite-frequency tomography of differential travel times between SS waves and their precursors.

2. Finite-Frequency Discontinuity Tomography

We use broadband seismograms recorded at GSN stations for earthquakes that occurred between January 2003 and September 2014. Instrument responses are removed and horizontal-component seismograms are rotated to obtain the radial- and transverse-component displacement seismograms. The transverse (SH) component seismograms are then band pass filtered between 0.01 and 0.1 Hz as SdS phases show best signal-to-noise ratio in this frequency range (Figure S1). To minimize possible interference between SdS waves and earthquake depth phases, we use earthquakes with focal depths shallower than 100 km. The moment magnitudes of the earthquakes range from 6.0 to 8.5 and the epicentral distances are between 90 and 160°. This raw data set contains about 150,000 traces.

To measure finite-frequency SS, S410S and S660S travel times, we carefully select seismograms with high-quality signals through visual inspection of each processed SH-component seismogram. The amplitude of an SS precursor depends on the size of the earthquake, source radiation pattern, the take-off angle and azimuth that determine the excitation of the S wave leaving the source as well as the reflection coefficient which depends on the epicentral distance. The amplitudes of the secondary reflected waves are small and often below the noise level, only about 30% of the recorded SS waves have clear SS precursors that are suitable for single-trace analysis. We compare observed seismograms with synthetic seismograms calculated in a 1-D reference earth model IASP91 (Kennett & Engdahl, 1991) using traveling wave mode summation (Liu & Zhou, 2016). Traces with highly deformed SS waveforms are not used in this study, including waveforms affected by complex rupture processes that are significantly different from synthetic seismograms. Travel time measurements are made with respect to IASP91 synthetic seismograms. The measurement time windows for SS waves (or their precursors) are determined based on the arrivals of the synthetic and the observed SS waves (or their precursors) (Figure S1). We choose time windows manually to ensure that the dominant energy of the measured phase is centered in the window. The length of the measurement window varies from 70 to 120 s. To obtain frequency-dependent travel time measurements, a cosine taper is applied in spectral estimates following the work of Deng and Zhou (2015). Finite-frequency effects in this data set and comparisons with ray-theoretical tomography have been documented in a separate study (Guo & Zhou, 2020). In this study, we focus on tomographic results based on measurements at 20 s period. Finally, we take advantage of calculated finite-frequency sensitivities in examining each measurement to identify possible complex wave interactions due to multiple phases arriving within a measurement window. This leaves a total of about 6,400 seismograms for 1,110 earthquakes, which provide good coverage in the oceans as well as in major subduction zones, except for in South America and its adjacent southern Pacific Ocean (Figure S2). The final data set does not show apparent geographic locations where data might be absent due to factors other than the source-receiver distribution.

We calculate finite-frequency sensitivities of SS and SdS traveltimes to boundary depth perturbations based on Born (single-scattering) approximation in the frame work of traveling-wave mode coupling (Deng & Zhou, 2015; Guo & Zhou, 2020; Zhou, 2009). Wave propagation simulations using the Spectral Element Method have shown that the finite-frequency sensitivities can account for diffractional effects of seismic body waves when depth variations of the 410-km and 660-km discontinuities are in the order of tens of kilometers (Deng & Zhou, 2015). The boundary sensitivity kernels fully account for source radiation patterns, phase interactions as well as time-domain windowing and tapering applied in making frequency-dependent measurements, which have been documented in a separate study (Guo & Zhou, 2020).

Travel time differences between observed and synthetic SdS waves ($\delta t|_{SdS}$) can be expressed as a two-dimensional integration over the global surface of the corresponding seismic discontinuity $\sum$

$$\delta t\,|_{SdS}\,(\omega) = \iint_{\Sigma} K_{\Sigma}^{SdS}(\mathbf{x},\omega)\delta d(\mathbf{x})d\Sigma, \tag{1}$$

where $K_{\Sigma}^{SdS}(\mathbf{x},\omega)$ is the sensitivity of an *SdS* travel time measurement at angular frequency ω to depth perturbations $\delta d(\mathbf{x})$ on the corresponding seismic discontinuity.

For SS waves, the relation can be written as

$$\delta t\,|_{SS}\,(\omega) = \iint_{\Sigma} K_{\Sigma}^{SS}(\mathbf{x},\omega)\delta d(\mathbf{x})d\Sigma. \tag{2}$$

The linear relation between measurements and discontinuity depth perturbations in Equations 1 and 2 guarantees

$$\delta t\,|_{SdS}\,(\omega) - \delta t\,|_{SS}\,(\omega) = \iint_{\Sigma}\left[K_{\Sigma}^{SdS}(\mathbf{x},\omega) - K_{\Sigma}^{SS}(\mathbf{x},\omega)\right]\delta d(\mathbf{x})d\Sigma. \tag{3}$$

Example boundary sensitivity kernels of SdS wave traveltime measurements and SdS-SS traveltime measurements are plotted in Figure S3. The finite-frequency sensitivities show a typical *X* shape due to the minimax-time nature of the reflected waves (Dahlen, 2005). The sensitivity of SS waves to the 410-km and 660-km discontinuity depth perturbation is about an order of magnitude smaller than the sensitivity of SdS waves. As a result, the sensitivity kernels for differential traveltime measurements ($\delta t|_{SdS} - \delta t|_{SS}$) show only minor differences from the sensitivity of SdS traveltimes ($\delta t|_{SdS}$) (Figure S3). We point out that due to wave interaction, the structure of sensitivity kernels is often more complex, depending on earthquake depths, epicentral distances as well as measurement windows.

We parameterize the surface of the Earth using a set of spherical triangular grid points with a lateral spacing of about 4° and the integration in Equation 3 is evaluated using 0.4° × 0.4° cells in the ray coordinate in which the source-receiver great circle path defines the equatorial plane. The tomographic problems are ill-posed and exact solutions do not exist, we solve a regularized least-square inverse problem

$$\|\mathbf{Gm} - \mathbf{d}\|^2 + \alpha^2\|\mathbf{m}\|^2 = \text{minimum} \tag{4}$$

where $\mathbf{G}$ is the kernel matrix, $\mathbf{m}$ is the model vector, $\mathbf{d}$ is the data vector and α is the Tikhonov regularization (norm damping). The minimization leads to

$$(\mathbf{G}^T\mathbf{Gm} - \mathbf{G}^T\mathbf{d}) + \alpha^2\mathbf{m} = 0. \tag{5}$$

We solve the above inverse problem based on singular value decomposition of matrix $\mathbf{G}$,

$$\mathbf{G} = \mathbf{U}\mathbf{\Lambda}\mathbf{V}^T. \tag{6}$$

where $\mathbf{\Lambda}$ is a rectangular diagonal matrix containing singular values λ_i, and $\mathbf{U}$ and $\mathbf{V}$ contain left and right singular vectors, $\mathbf{u}_i$ and $\mathbf{v}_i$, respectively.

The Tikhonov solution of the inverse problem can be written as

$$\mathbf{m} = \sum_{j=1}^{p} \left(\frac{\lambda_j^2}{\lambda_j^2 + \alpha^2} \right) \frac{\mathbf{u_j}^T \mathbf{d}}{\lambda_j} \mathbf{v}_j, \tag{7}$$

where p is the rank of the singular value matrix.

The corresponding resolution matrix is

$$\mathbf{R} = \mathbf{VFV}^T, \tag{8}$$

where $\mathbf{F}$ is diagonal matrix with elements $\lambda_j^2 / \left(\lambda_j^2 + \alpha^2 \right)$. The tradeoff between data misfit and model norm for different regularization parameter α as well as resolutions of the optimal models are plotted in the Supplemental Figures (Figures S4–S6). The 410-km and 660-km discontinuities are obtained from separate inversions using their respective measurements. The thickness of the MTZ from this data set has been discussed in Guo and Zhou (2020). In this study, we focus our discussions mostly on the correlation between the 410-km discontinuity and the 660-km discontinuity depth perturbations as it is less sensitive to different regularization parameters used in the inversions.

Lateral variations in crustal structure as well as wave speed variations in the bulk mantle may introduce travel time shifts on SS and SdS waves. We calculate crustal corrections based upon traveltime differences between IASP91 models with and without a global crustal structure, CRUST 1.0 (Laske et al., 2013). The crust is 20 km thick in the reference model IASP91 and maximum crustal corrections using model CRUST1.0 are about 5 s for SS waves reflected off the Tibetan Plateau where the thickness of the crust reaches about 80 km. Overall, the SdS-SS differential measurements at 20 s period with and without crustal corrections show minor differences. We calculate 3-D mantle wavespeed corrections using two existing global models, S40RTS (Ritsema et al., 2011) and S362ANI+ M (Moulik & Ekström, 2014). The choice of mantle model in wavespeed corrections does not affect major structures in discontinuity. It has been pointed out, based on modeling using the spectral element method, that the amplitudes of discontinuity depth variations may be underestimated when ray theory corrections are used for time-domain cross-correlation measurements (Koroni & Trampert, 2016). For frequency domain cosine-taper measurements, wave propagation simulations show that depths of mantle discontinuities can be reasonably well recovered when ray theory corrections are made (Deng & Zhou, 2015). We focus on mantle wave speed corrections based on model S40RTS in this study. Models obtained using S362ANI+M corrections have also been included in the Supplemental Figures for reference.

3. Results

3.1. The 410 and the 660 in Subduction Zones

The most striking feature in the discontinuity maps is large-scale depressions in both the 410-km and 660-km discontinuities around the Pacific subduction zones (Figure 1). The circum-Pacific distribution of the positive correlation is best illustrated by the *correlational sum* in (c) and (f). In regions where both discontinuities experience depressions, the *correlational sum* is positive (in blue) and its magnitude is the sum of the absolute depth perturbations of the two discontinuities. Travel time corrections made using existing crust and bulk mantle models do not affect the general positive correlation along the circum-Pacific subduction zones (Figures 1 and S7). The global data distribution is not uniform but shows reduced coverage in Africa, South Asia and Northwest Australia and minimum data sampling in South America and adjacent oceans (Figure S5). In South America where stagnant slabs have been imaged in the MTZ, the 410-km and 660-km discontinuities are both significantly deeper in regional studies (e.g., Schmerr & Garnero, 2007). In Figure S6, resolution tests on the 410-km and 660-km discontinuity models using spherical harmonic "checkerboard" at two different length scales ($l = 12$ and $l = 20$) show that structures are well resolved in Eurasia, North America, the Pacific Ocean and the Indian Ocean, consistent with the sensitivity density (diagonal elements of the matrix $\mathbf{G}^T\mathbf{G}$) and diagonal elements of the resolution matrix (Figure S5).

The strong positive correlation in the Pacific subduction zones is somewhat counter-intuitive, because thermal variations due to a cold slab in the MTZ would predict an "anti-correlation" between the two

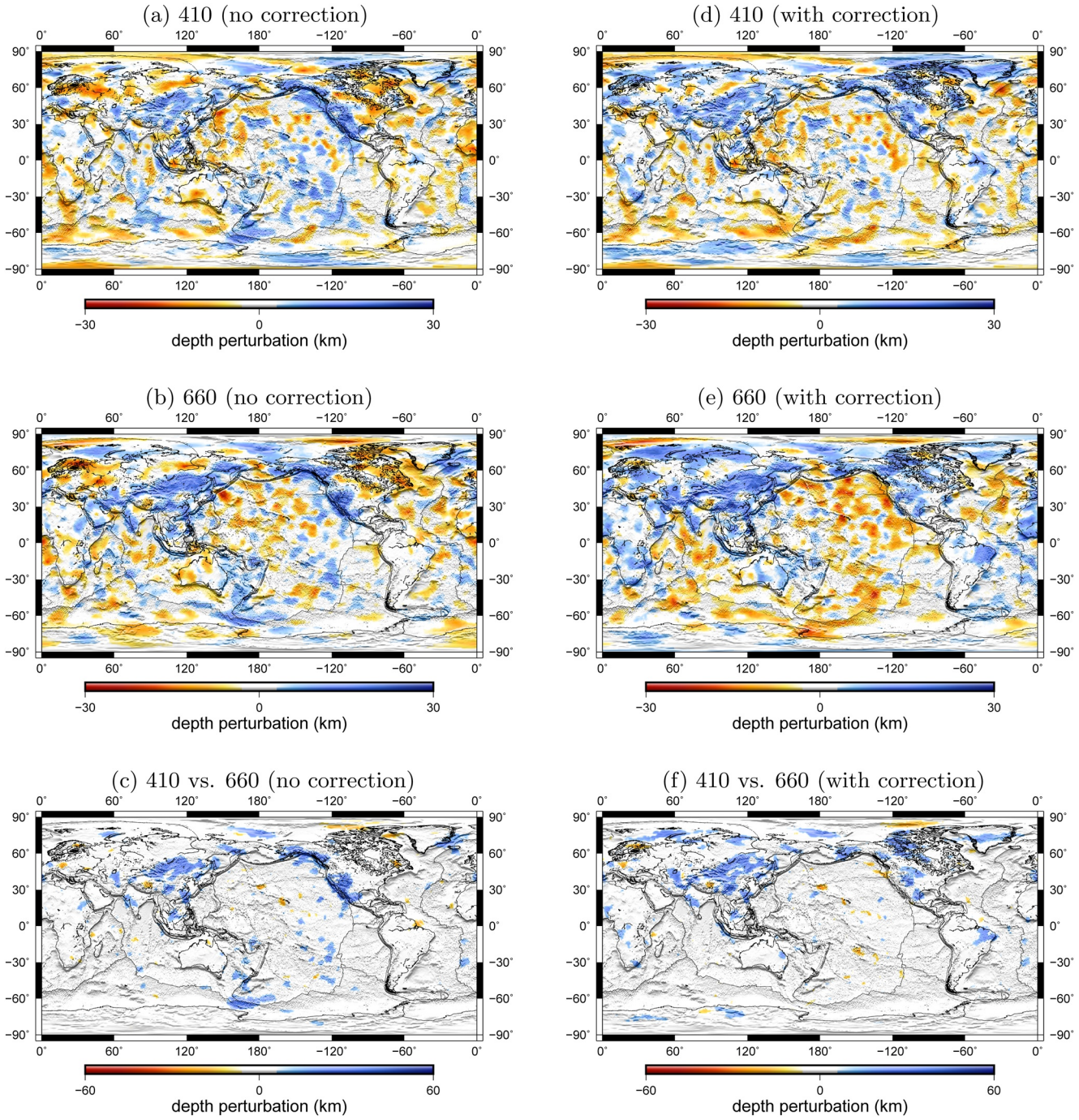

Figure 1. Global models of the 410 and the 660 from finite-frequency discontinuity tomography. (a and b) are global depth perturbations of the 410-km and 660-km discontinuities imaged from finite-frequency tomography of S410S-SS and S660S-SS differential traveltime measurements. (c) *correlational sum* with its magnitude defined as the sum of the absolute perturbations of the 410 and the 660. It is positive (blue) in regions where both discontinuities occur at depths greater than the global average; and it is negative (red) in region where the 410 is deeper while the 660 is shallower (typical anti-correlation signature for mantle plumes). The *correlational sum* is not defined (zero) in other regions. Only regions with both discontinuity depth perturbations larger than uncertainties (5 km) are plotted. (d–f) are the same as (a–c) but models obtained using traveltime measurements corrected for 3-D seismic structure in the crust (CRUST1.0) as well as wavespeed variations in the mantle (S40RTS). Due to uncertainties in the global crust and mantle wavespeed models, we will focus on features that are consistent before and after the corrections.

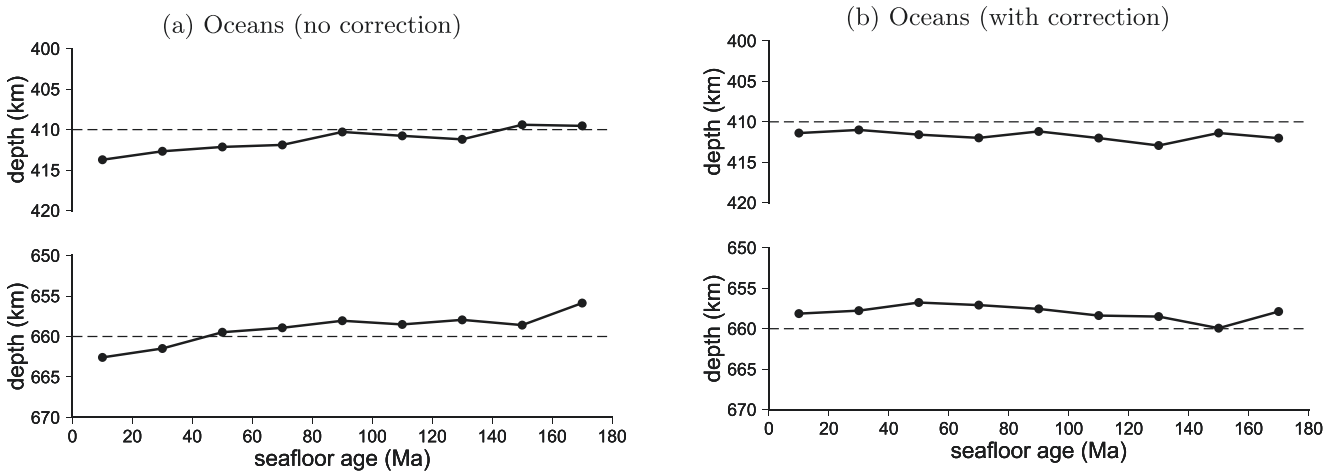

Figure 2. The 410 and the 660 in oceanic regions. (a) depth perturbations of the 410 and the 660 in global oceanic regions, averaged over every 20-million-year age band; (b) the same as (a) but for models inverted using traveltime data corrected using model CRUST1.0 and S40RTS.

discontinuities for a vertically dipping slab or no correlation if the slab stagnates above the 660. This positive correlation has not been reported in previous global models (Gu et al., 2003; Houser et al., 2008; Lawrence & Shearer, 2008) but it is in general agreement with several regional scale studies based on SS precursors and receiver functions (e.g., Heit et al., 2010; Shen et al., 2008). However, interpretations in regional studies have been difficult as this positive correlation is not expected in the general context of subduction. The global distribution of the MTZ discontinuity anomalies indicates a general subduction origin associated with stagnant slabs, possibly warm return flows from the lower mantle filling the space above a stagnant slab as it gradually sinks into the lower mantle.

In other subduction zones, the correlation between the 410-km and 660-km discontinuity depth perturbations is much weaker (Figure 1). The lack of positive correlation between the 410 and the 660 in the Alpine-Tethys region is consistent with recent regional studies where most of the Tethyan lithosphere probably has sunk down to the lower mantle (Hafkenscheid et al., 2006). The 660-km discontinuity anomalies show similar structure to wave speed anomalies in the lower MTZ along the Tethyan suture zone, extending from the Mediterranean through the northern Middle East into the Tibetan Plateau (Schaeffer & Lebedev, 2013). The 410-km discontinuity anomalies are much weaker and smaller in lateral extent, indicating the absence of large-scale return flows warming up the shallower mantle. In the Philippine trench and the Sunda trench, discontinuity anomalies are narrow features in the close proximity to current trench, consistent with steep penetration of subducted slabs across the MTZ without much flattening above the 660-km discontinuity (Dokht et al., 2018; Hall & Spakman, 2015). It is worth noting that the anti-correlation can also be found in some areas where slabs are absent, but they are in general smaller in size and/or sensitive to velocity corrections. In this study, we shall focus only on the most robust features.

3.2. The 410 and the 660 in Oceanic Regions

In oceanic regions, there was an age-dependent signature with both the 410 and the 660 becoming shallower as the seafloor gets older (Figure 2a). This pattern was introduced by slower S-wave speed in the upper mantle beneath younger seafloors in response to seafloor spreading, and, the age-dependence is removed after mantle wave speed corrections are applied (Figures 2b and S8). The average depths of the 410-km and 660-km discontinuities are about 411 and 658 km, respectively. Overall, the oceanic MTZ is about 3 km thinner than the global average and it does not show significant variations with seafloor age. The overall thinner MTZ and slower seismic wave speed at those depths in global models (Moulik & Ekström, 2014; Ritsema et al., 2011; Schaeffer & Lebedev, 2013) suggest the existence of far-field return flows in the global oceanic mid mantle. The convection process is probably complex as the discontinuity structures in oceanic regions also show strong small-scale variations (Figure 1).

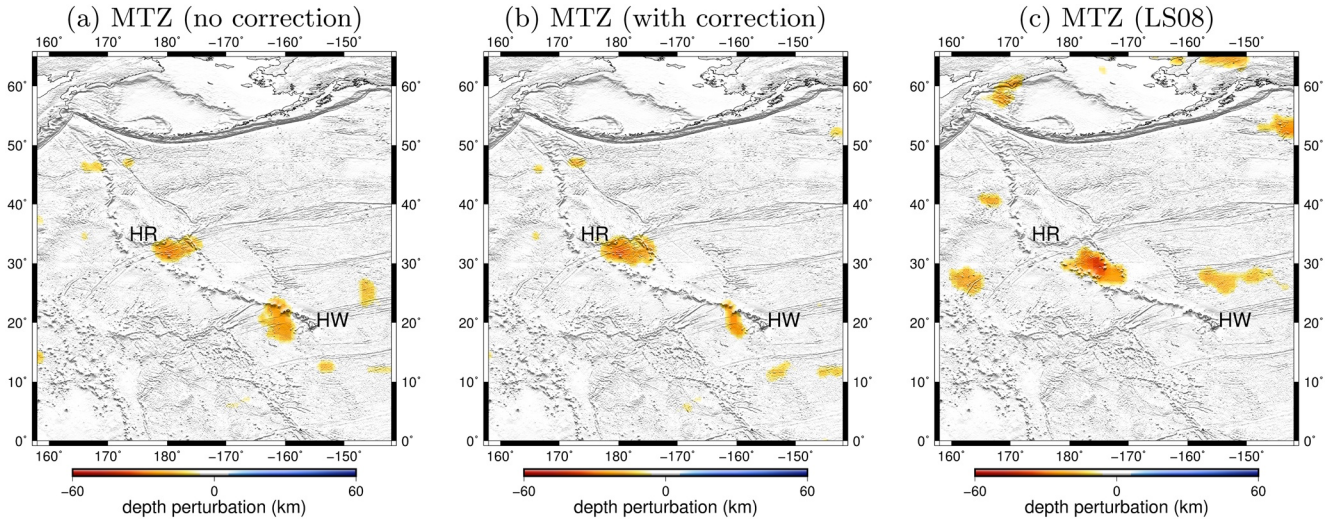

Figure 3. (a and b) are the *correlational sum* of the 410 and the 660 in the Pacific (same as Figures 1c and 1f); (c) *correlational sum* calculated using discontinuity models published by Lawrence and Shearer (2008). The anomaly west of the island of Hawaii (HW) becomes much weaker after wave speed corrections. The *plume-like* structure south of Hess Rise (HR) is a consistent feature in all three models.

In Figures 1c and 1f, the plume-like structures in the Pacific Ocean are characterized by an anti-correlation between the 410 and the 660 (negative correlational sum), and they show significant differences in models with and without mantle wave speed corrections. For example, the correlation at the South Pacific Superswell changes polarity after wavespeed corrections. A plume-like anomaly west of the island of Hawaii becomes much weaker after wave speed corrections (Figure 3). Plume anomalies are in general much smaller in lateral extent compared to slab anomalies, therefore, they are less well resolved due to limited spacial resolution in this study. In addition, linearized velocity corrections may have an impact (Koroni et al., 2019; Koroni & Trampert, 2016), therefore, we do not attempt to interpret weak plume anomalies at a global scale but only focus on the most prominent anomalies. The only significant plume-like signature in the discontinuity models regardless of wave speed corrections is located south of Hess Rise. In examining published models, we noticed the anomaly was also present in an earlier global finite-frequency model but the anomaly was not discussed (Lawrence & Shearer, 2008). While the size of the anomaly is close to the resolution limit in our model (Figure S6), the general agreement among those models suggests that this anomaly south of Hess Rise is reasonably well resolved. The geoid anomaly in this region also indicates a possible mid-mantle origin (Sandwell & Renkin, 1988; Wessel et al., 1994). Hess Rise was formed sometime in the early Cretaceous (Vallier et al., 1980). The relation between recent deep mantle convection processes and the evolution of the oceanic plateau remains unclear. We point out that the plume-like features indicate possible small-scale upwellings through the MTZ, not necessarily that they originate from the core-mantle boundary. Similar small negative anomalies can also be found in Tibet and Northern Europe (Figure 1).

In this study, we have focused our discussions on the polarity of the 410-km discontinuity and the 660-km discontinuity depth perturbations as it is less sensitive to the damping parameter (α) used in the inversions than the absolute amplitude. The MTZ discontinuities have been modeled as first-order discontinuities. In reality, velocity structures are more complicated and may include gradient zones and thin layers. For example, thin melt layers with a horizontal extent of about a couple of hundred kilometers have been reported above the 410-km discontinuity in East Asia and the Alps, possibly caused by local water transport out of the MTZ (Z. Liu et al., 2016, 2018). At 20 s period, our inversion results are not sensitive to detailed wave speed structure but rather represent the depths of the equivalent first-order discontinuities (Deng & Zhou, 2015). The tradeoff between resolution and model uncertainty depends on noise levels in the measurements as well as the sensitivities of travel times to depth perturbations, which are different for S410S and S660S waves. The damping parameter affects the amplitudes of the recovered depth perturbations, however, the polarity (uplift or depression) is well resolved in both models. For example, the 410 and the 660 are both deeper than the global average in subduction zones, this is well resolved but the magnitude of their depressions might have been underestimated.

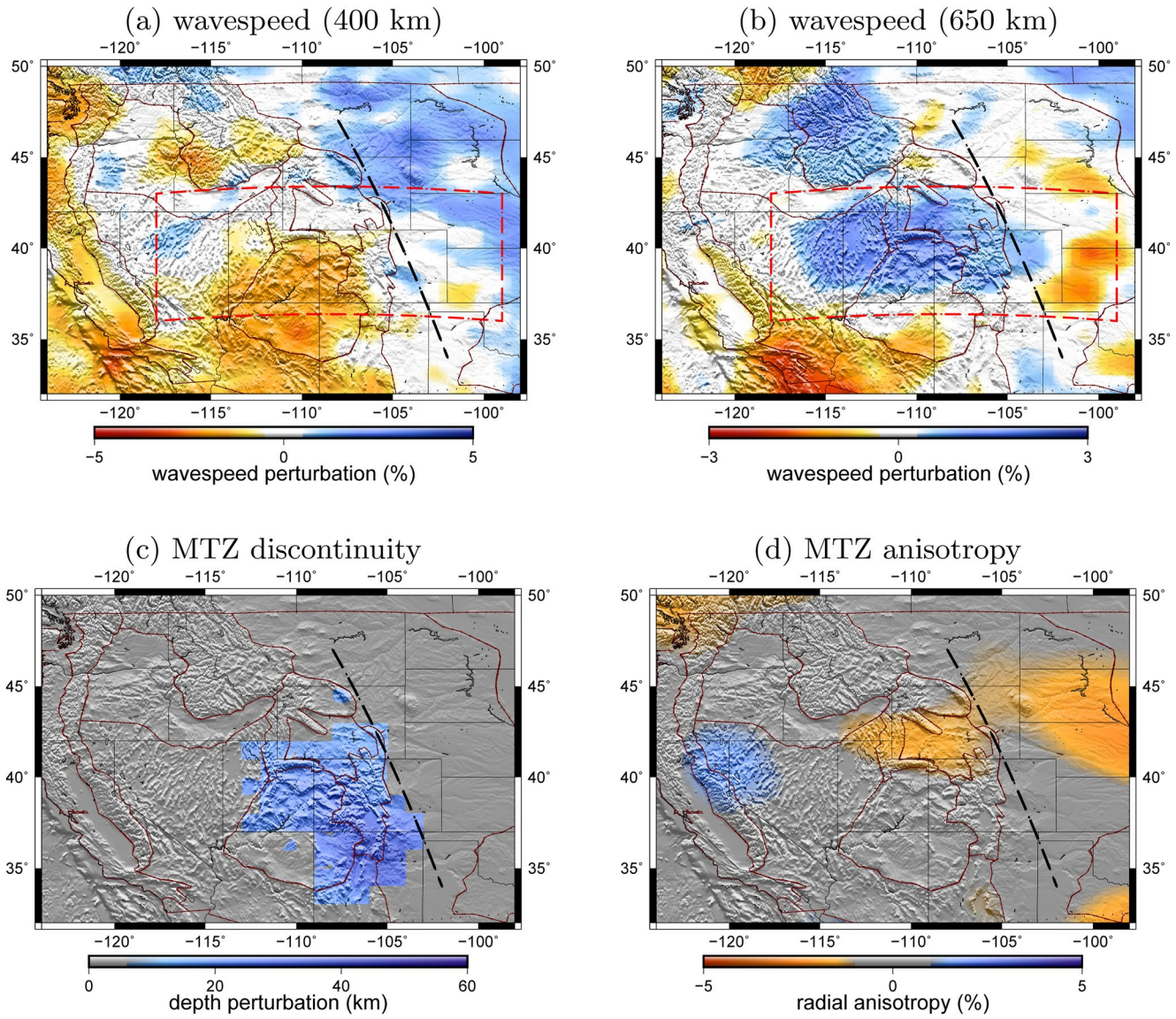

Figure 4. Warm mantle above stagnant slab in the Western US. (a and b) are S-wave velocity perturbations at 400 and 650 km depths, respectively (Tian et al., 2011). (c) *correlational sum* of the 410 and the 660 in the Western US with positive values in regions where both the 410 and the 660 occur deeper than the global average. Only regions with consistent anomalies in Figures 1c and 1f are plotted. (d) average radial anisotropy in the mantle transition zone (MTZ) in model US22 (Zhu et al., 2017) where negative ($V_{SH} < V_{SV}$) radial anisotropy indicates dominant vertical mantle flow. Dark red lines are major geological boundaries; black dashed line indicates subduction front in the MTZ. The 3-D wavespeed model in the red box in (a and b) is plotted in Figure 5.

4. Discussions

In the western United States, the unprecedented deployment of EarthScope USArray allows us to take advantage of high-resolution wave speed tomographic models in this region together with the MTZ discontinuity models to investigate the thermal structure in the MTZ. The overall depressed 410-km and 660-km discontinuities are in general agreement with recent regional studies using USArray receiver functions (Gao & Liu, 2014; Wang & Pavlis, 2016; Y. Zhou, 2018). In seismic wave speed tomography, fast slab anomalies have been imaged in the lower MTZ from Idaho and Western Montana down to Utah and Colorado (Sigloch et al., 2008; Tian et al., 2011). In the upper MTZ, this region is dominated by seismic slow (warm) anomalies (Figure 4). The overall anti-correlation between wave speed perturbations in the upper and lower MTZ in the western United States supports a thermal origin of the observed discontinuity perturbations. Nonthermal origins such as water content have been proposed to explain low seismic wavespeed anomalies at the

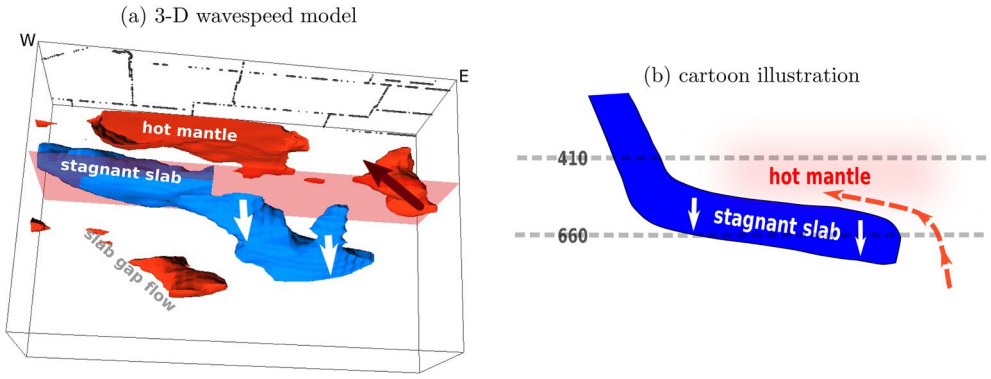

Figure 5. 3-D wavespeed structure in the Western US and Cartoon illustration of subduction with stagnant slab. (a) 3-D rendering of S-wave slab anomalies in the Western US. The isosurface represents 1% fast and slow seismic wavespeed anomalies at depths from 50 to 1,600 km (Tian et al., 2011). US State boundaries are plotted at the surface for geographic reference. Fast anomalies in the upper mantle beneath the craton have been removed for better illustration of the slab. (b) Cartoon (not to scale) illustrating the sinking of a stagnant slab from the mantle transition zone (MTZ) into the lower mantle. The 660-km discontinuity occurs deeper (not illustrated) due to the cold stagnant slab in the lower MTZ and the 410-km discontinuity also occurs at greater depths (not illustrated) due to warm return flows in a super adiabatic mantle.

top of the MTZ, however, the positive correlation between the 410 and the 660 in this region cannot be explained by slab hydration because increased water content would lead to a shallower 410-km discontinuity (Smyth & Jacobsen, 2006). We point out that wavespeed and discontinuity anomalies at those depths do not show exact correspondence in their locations, due to the 3-D nature of the slab geometry as well as differences in data sensitivity and coverage, model parametrization and resolution.

The stagnation of the subducted Farallon plate at the 660-km discontinuity and a warm mantle above the slab is better illustrated in the 3-D wavespeed image in Figure 5. To balance the sinking of a stagnant slab into the lower mantle, it requires an ascending return flow from the lower mantle. The overall much warmer upper MTZ indicates the poloidal mode of mass exchange occurs in the close proximity of the descending slab. Recent geodynamic modeling and fabric calculation suggest that lattice preferred orientation can explain observed seismic anisotropy in the MTZ (e.g., Sturgeon et al., 2019). To the east (ahead) of the subduction front, wavespeed and radial anisotropy indicate the presence of local upwellings from the lower mantle (Figures 4 and 5). The upwellings are confined in the MTZ and "feed" the slow anomalies above the stagnant slab. We interpret the upwellings as return flows in a superadiabatic mantle, driven by the sinking of the stagnant slab. In reality, subduction can be much more complicated than the simplified cartoon illustration in Figure 5 due to complex processes such as slab fragmentation and the evolution of multiple subduction systems through time (Sigloch et al., 2008). In the Western US, it has been suggested that the mode switch from stagnation to penetration is possibly associated with reversed polarity subduction of a section of slab between preexisting fracture zones on the Farallon plate, which generates a return flow through the slab gap, producing the Yellowstone volcanoes (Y. Zhou, 2018). In this global study, we do not have the spatial resolution to investigate complex structures of slabs.

In Eastern Asia, this strong positive correlation extends about 3,000 km westward inland from the present-day Ryukyu trench, with a gap roughly beneath the North China Craton (Figure 6). This positive correlation between the 410-km and 660-km discontinuity topography largely agrees with wavespeed anomalies in the mid mantle (Schaeffer & Lebedev, 2013), where slow wavespeed dominates this region in the upper MTZ (~400 km) while fast anomalies are imaged in the lower MTZ (~650 km). Regional observations made on SS precursors also suggest the existence of reduced seismic wavespeed in the upper MTZ and depressions on the 410-km and 660-km discontinuities (Heit et al., 2010). The overall agreement indicates that the dominant mechanism associated with depth perturbations of the two discontinuities is also thermal. Radial anisotropy in the MTZ is consistent with local upwellings at the leading side (west) of subduction, and the anomalies are also largely confined in the MTZ (Chang et al., 2014). The global wave speed model shown in Figure 6 was obtained using multimode surface waves, which provide improved sensitivities down to the

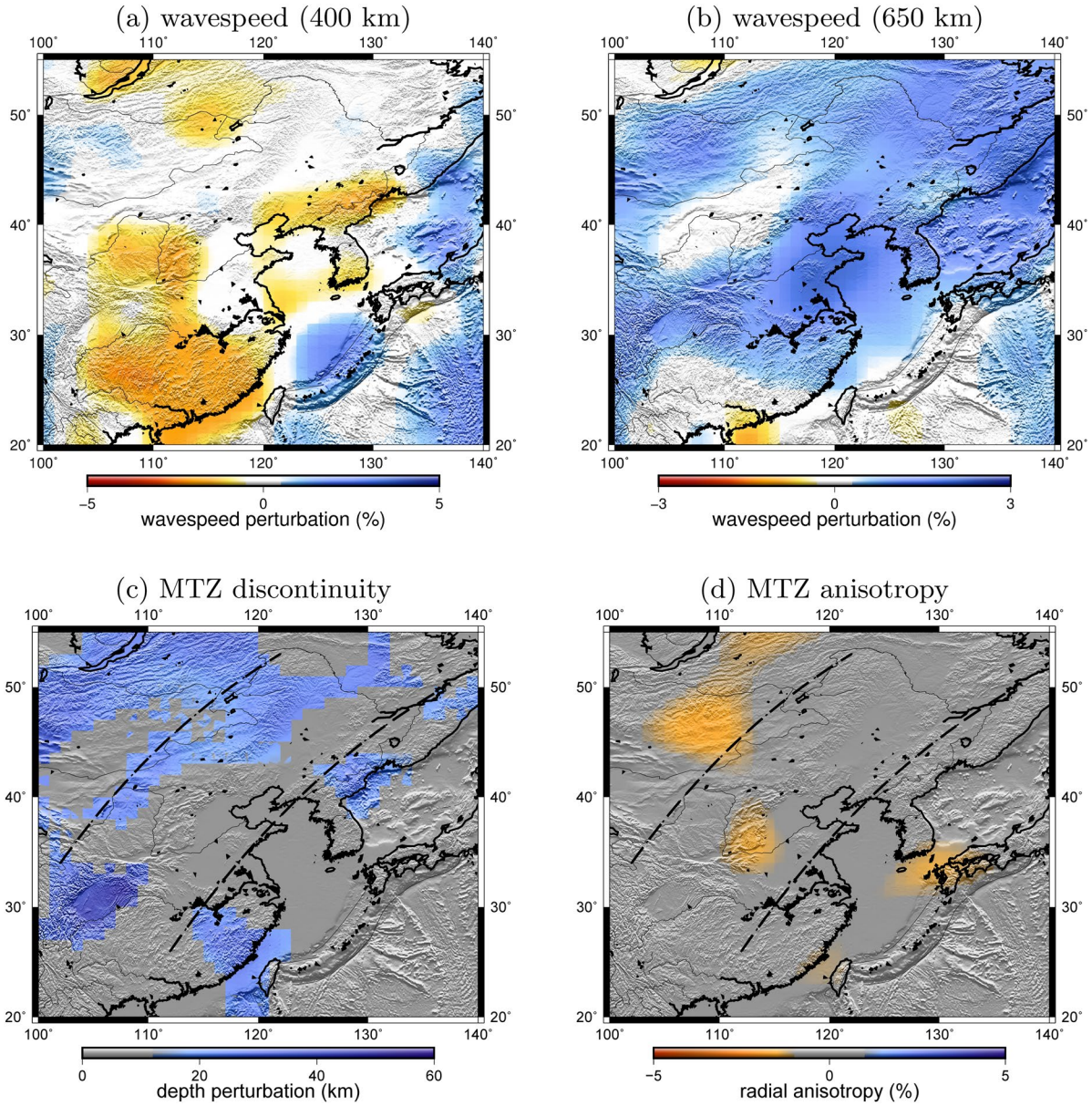

Figure 6. Warm mantle above stagnant slab in Eastern Asia. (a and b) are S-wave velocity perturbations at depths of 400 and 650 km from Schaeffer and Lebedev (2013). (c) *correlational sum* of the 410 and the 660 in Eastern Asia, only regions with consistent anomalies in Figure 1c and 1f are plotted. (d) average radial anisotropy in the mantle transition zone (MTZ) in model SGLOBE-rani (Chang et al., 2014), where negative radial anisotropy ($V_{SH} < V_{SV}$) indicates dominant vertical mantle flow. Two dashed lines indicate subduction systems in the MTZ, roughly parallel to the present-day Ryukyu trench.

MTZ. While stagnant slab anomalies are a common feature in this region in wave speed tomographic models (Moulik & Ekström, 2014; Schaeffer & Lebedev, 2013; Tao et al., 2018), we point out that the geometry of wavespeed anomalies vary considerably at those depths among those models.

The large-scale MTZ discontinuity anomalies show two structures separated by a gap in the North China Craton. The gap is oriented in northeast direction, roughly parallel to the present-day Ryukyu trench. We interpret this structure as a result of stagnant slabs from two subduction systems, the current subduction of the Philippine sea plate which deposited slab materials east of the gap, and an earlier subduction of the Pacific plate beneath the Eurasia plate which deposited slab materials west of the North China Craton. The subduction of the Pacific plate in this region ceased about 40 million years ago as the growing Philippine sea plate moved northward into the place (Hall, 2012; Seno & Maruyama, 1984).

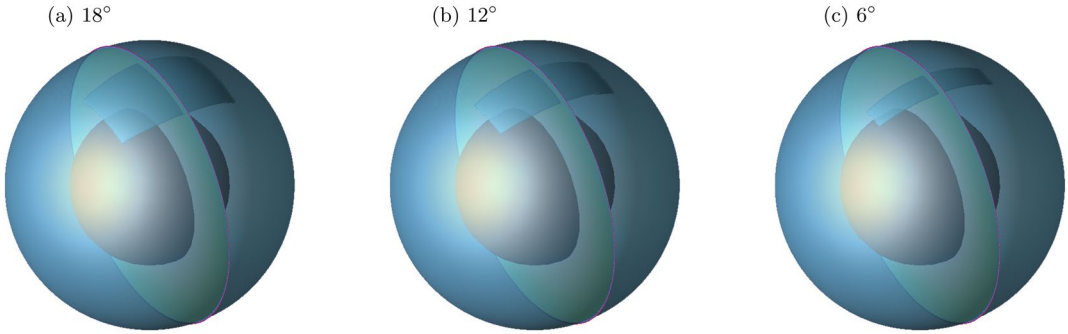

Figure 7. Geometry of the stagnant slab in the mantle transition zone (MTZ) in CitcomS simulations. The width of the slab is 60° and the stagnation half-length is 18° in (a), 12° in (b) 6° in (c).

5. Geodynamical Simulations

We examine the convection dynamics of a stagnant slab in the MTZ using CitcomS (Tan et al., 2006; Zhong et al., 2000, 2008). We assume slab stagnation is transient (U. R. Christensen, 1996; Mao & Zhong, 2018) and focus on passive upwellings produced by a massive free-sinking slab at the depths of the MTZ due to its negative thermal buoyancy (Figure 7). The simplified model has a stagnant slab that is initially detached from the shallower lithosphere and modeled as a temperature anomaly with a latitude extent (width) of 60° and a thickness of 160 km. We vary the stagnation length of the slab (longitude extent) and examine return flows as a function of distance from the slab center.

We use CitcomS (Tan et al., 2006; Zhong et al., 2000, 2008) to simulate mantle convection in an incompressible 3D spherical shell under the assumptions of the Boussinesq approximation. The nondimensional governing equations for the conservation of mass, momentum and energy are

$$\nabla \cdot \mathbf{u} = 0 \tag{9}$$

$$-\nabla P + \nabla \cdot [\eta(\nabla \mathbf{u} + \nabla^{\mathrm{T}}\mathbf{u})] + RaT\mathbf{e}_r = 0 \tag{10}$$

$$\frac{\partial T}{\partial t} + \mathbf{u} \cdot \nabla T = \nabla^2 T \tag{11}$$

where $\mathbf{u}$ is the velocity vector, P is dynamic pressure, η is viscosity and $\mathbf{e}_r$ is the unit vector in the radial direction. T is temperature, t is time, and Ra is the Rayleigh number,

$$Ra = \frac{\alpha \rho g \Delta T R^3}{\eta_0 \kappa}, \tag{12}$$

where α is thermal expansion coefficient, ρ is density, g is the gravitational acceleration, ΔT is the temperature difference across the mantle, R is the radius of the earth and κ is thermal diffusivity. The subscript 0 denotes reference values. Thermodynamic parameters are constants (Table 1) except for the viscosity.

Table 1
Thermodynamic Parameters

Parameter	Value	Unit
Earth's radius R	6,371	km
Gravitational acceleration g	10	m/s^2
Mantle density ρ	4,000	kg/m^3
Thermal expansion coefficient α	2.0×10^{-6}	K^{-1}
Temperature difference ΔT	2,500	K
Reference viscosity η_0	10^{22}	P a·s
Specific heat capacity	1,200	J/k g·K

The nondimensional rheological equation for depth- and temperature-dependent viscosity is (X. Liu & Zhong, 2016)

$$\eta = \eta'(r)\exp[E(0.5 - T)] \tag{13}$$

where $\eta'(r)$ is a depth-dependent viscosity pre-factor with a four-layer structure, and their ratios in the lithosphere, upper mantle, MTZ and lower mantle are $\eta'_{lith} : \eta'_{upper} : \eta'_{tz} : \eta'_{lower} = 10 : 0.01 : 0.1 : 3$. It has been suggested that a four-layer mantle viscosity structure with a high-viscosity

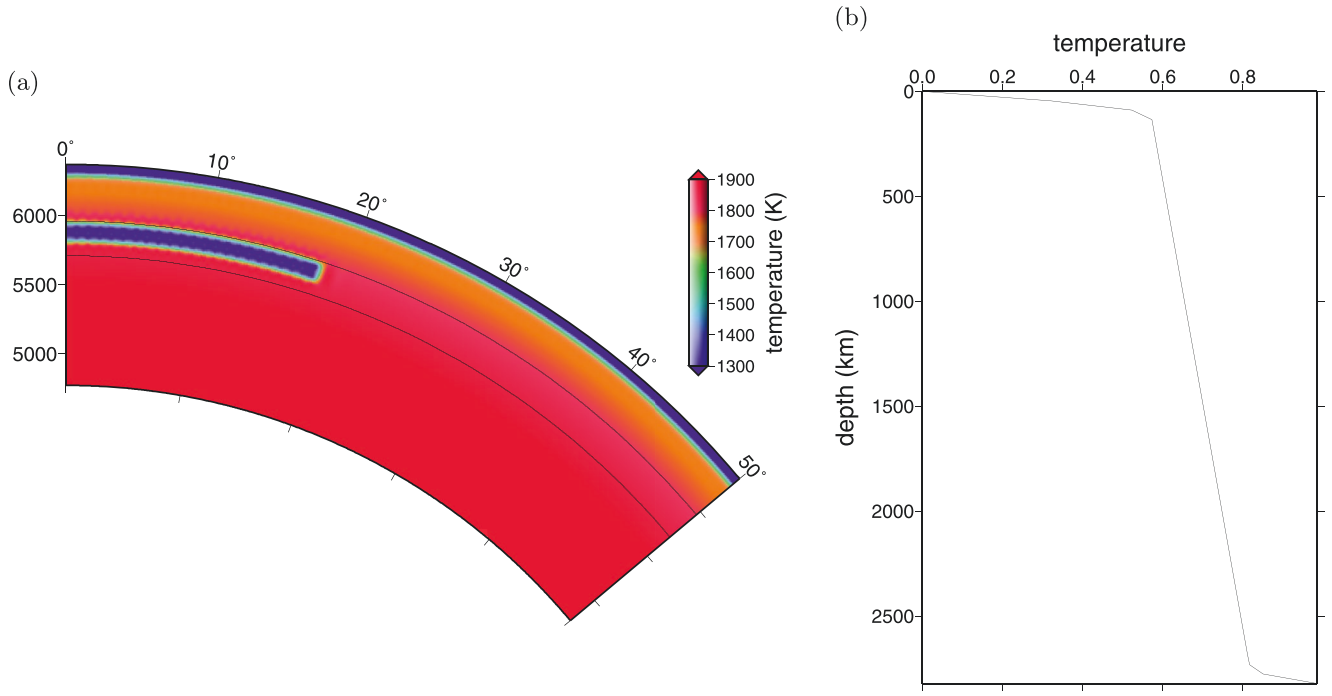

Figure 8. (a) cross-section view of the initial temperature field (stagnation half-length = 18°). The vertical axis is radius (in km). (b) nondimensionalized temperature as a function of depth.

lid (lithosphere), a low viscosity upper mantle (asthenosphere) and an increase in viscosity in the MTZ fit the geoid data better than a simple two-layer (upper-mantle and lower mantle) parametrization of viscosity (e.g., Hager & Richards, 1989; van Keken & Zhong, 1999; Xue & King, 2016). The radial temperature profile is plotted in Figure 8. As we will focus on return flows beneath continents where stagnant slabs have been imaged, the thickness of the lithosphere is 200 km in all simulations. The 410-km and the 660-km discontinuities are modeled as viscosity boundaries but the effects of phase changes have been neglected.

To obtain moderate viscosity variations in the mantle, we have used relatively small activation energy values (Zhong et al., 2000) with $E = 6.9$ above the 660-km discontinuity and 3.6 in the lower mantle in the cases of temperature-dependent viscosity (cases I and III). The activation energy $E = 0$ in cases II and IV where viscosity is constant is each layer (Figure 9). Thermal insulation of continents may facilitate melting in the continental asthenosphere (Till et al., 2010). It has been reported in mineral physics experiments that the viscosity of partial melts decreases with increasing depth in the upper mantle (Kushiro, 1986), and a melt layer atop the 410-km discontinuity has been observed in continental regions based on seismic receiver function (Tauzin et al., 2010) and electromagnetic studies (Toffelmier & Tyburczy, 2007). We examine return flows in the presence of a local low viscosity layer in the upper mantle at depths between 300 and 400 km in cases I and II (Figure 9).

In Figure 10, we show the temperature and flow field from simulations for different sizes of stagnant slabs. The simulations show that return flows produced by a sinking slab are localized in the vicinity of the descending slab. We calculate the radial flow flux in every 1°×1° degree cell and then we integrate it over latitude from −90° to 90° and plot it as a function of distance normalized by stagnation half length. The vertical mass exchange between the upper mantle and lower mantle is better illustrated by the radial velocity and flow flux in the MTZ as a function of distance from the slab center. As the longitude extent (stagnation) of the slab increases, it does not produce a broader area of upwellings but only stronger return flows near the slab, regardless of viscosity structures used in the simulations (Figure 11). The strength of the return flow depends on the size of the slab, when the width of the slab reduces to 12°, local return flows become largely absent (Figure 12). In all simulations, variations in activation energy do not have a major impact on the pattern of the return flow. As the stagnation length increases, the return flow becomes stronger but confined in the vicinity of the slab (Figures 10 and 11).

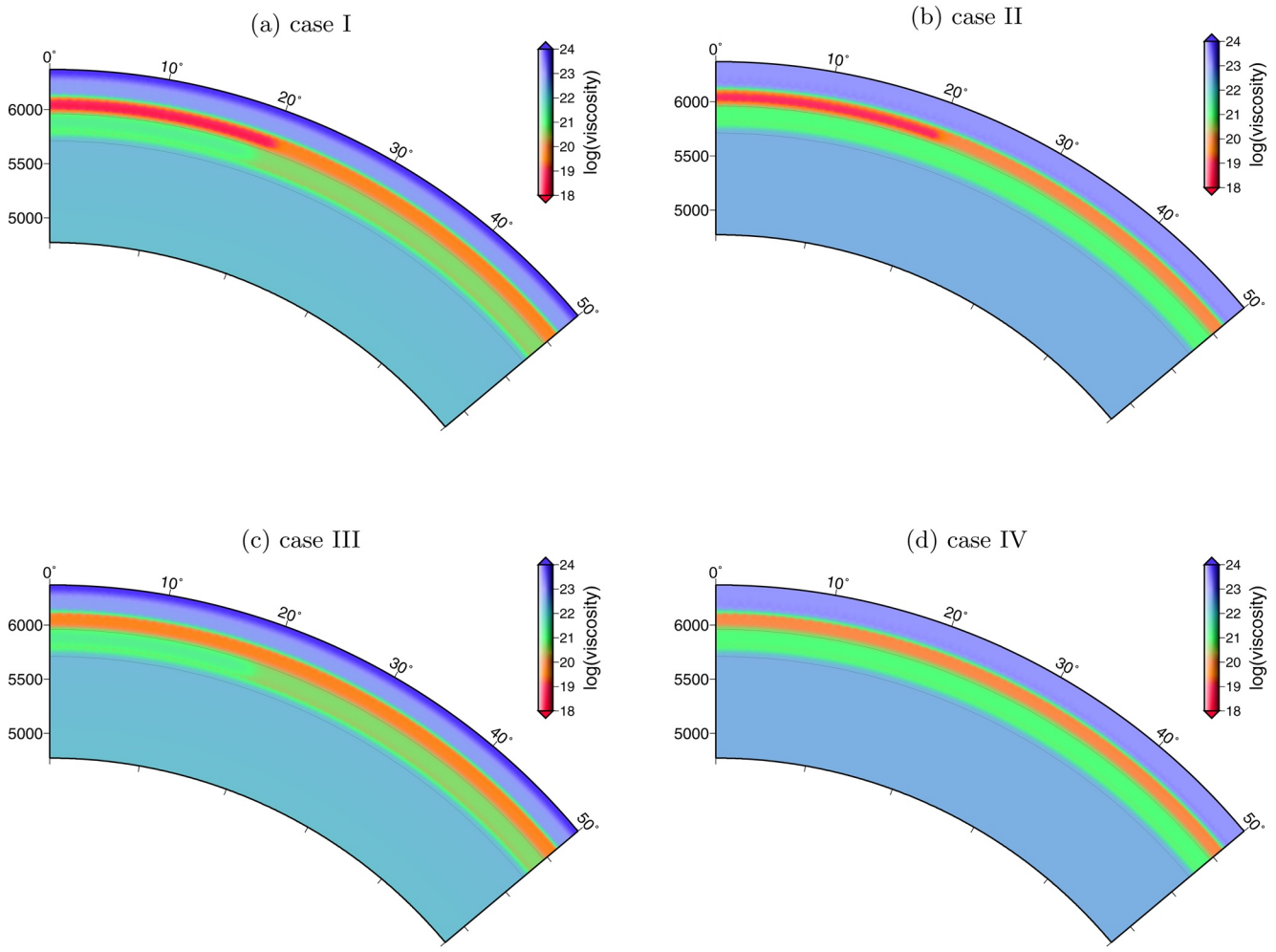

Figure 9. cross-section views of viscosity structures used in CitcomS simulations. The slab stagnation half-length is 18° in all plots. In cases I and III, viscosity is temperature dependent, and in cases II and IV, viscosity is constant in each layer. In cases I and II, a local low viscosity layer is introduced in the continental asthenosphere above the stagnant slab at depths between 300 and 400 km.

It is generally assumed that the Earth's mantle is only slightly deviated from adiabatic (Birch, 1952; Dziewonski & Anderson, 1981). The adiabatic mantle temperature gradient is ~0.3 K/km (Turcotte, 2002) while it has been suggested that a super-adiabatic temperature gradient of 0.4–0.6 K/km in the lower mantle would fit seismic and electromagnetic data better than an adiabatic mantle (e.g., Khan et al., 2006; Verhoeven et al., 2009). In the simulations, we have used a super-adiabatic temperature gradient of ~0.2 K/km in the bulk mantle and the return flows warm up the shallower MTZ above the slab by about 75°K. We emphasize that the adiabatic mantle temperature gradient (which does not drive convection) is not considered in incompressible models. If we assume a Clapeyron slope of ~3 MPa/K for the olivine to wadsleyite phase transformation, this temperature change corresponds to ~6–7 km of depth perturbation on the 410-km discontinuity. In the Pacific subduction zones where large-scale stagnant slabs have been imaged in the MTZ, the average depth perturbation is ~9–10 km. While the return flows in a superadiabatic mantle may account for the majority of the deflections of the 410-km discontinuity, other contributing effects may not be neglected. For example, the subduction of the Farallon plate may have brought hot materials from the Pacific upper mantle into western North America (Q. Zhou et al., 2018). In addition, thermal blanketing beneath the stable continents may also increase the temperature of the asthenosphere above the stagnant slab (Till et al., 2010). The return flows rising from the lower mantle may be rich in harzburgite in the presence of chemical layering (Ballmer et al., 2015; Nakagawa & Buffett, 2010), resulting in more seismically visible deflections of the discontinuities (Nakagawa & Buffett, 2010; Xu et al., 2008). In the future, it would also

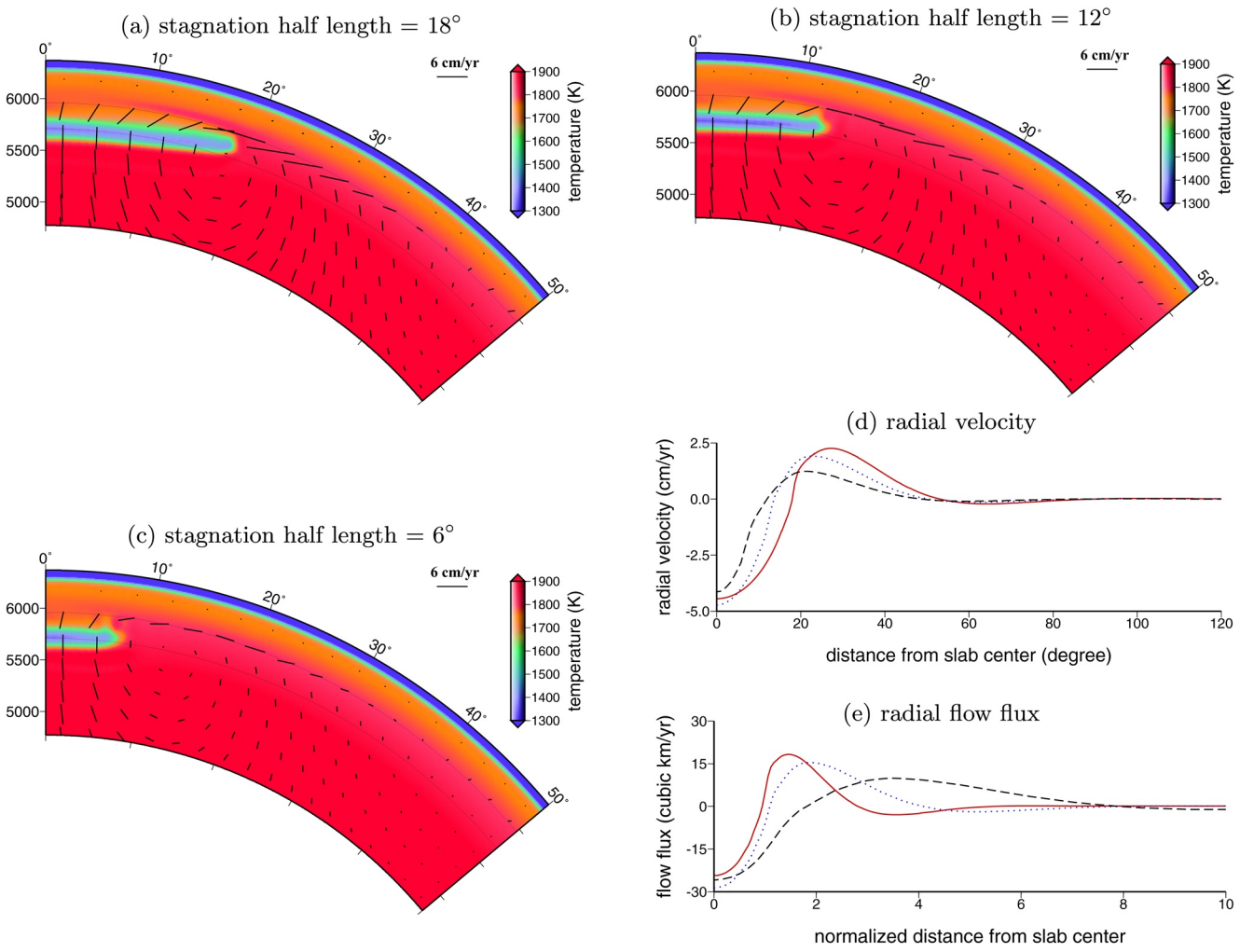

Figure 10. CitcomS simulations of a stagnant slab in the mantle transition zone (MTZ) sinking into the lower mantle. The return flows are localized in the vicinity of the slab, regardless of the stagnation length. (a–c) are cross-sections of the temperature and flow field for slabs with different stagnation extent in the MTZ. The slab geometries and initial conditions are plotted in Figures 7 and 8 and the viscosity structure is plotted in Figure 9a. (d) is the radial (vertical) velocity at a depth of 630 km as a function of distance from the slab center in the three cross-sections: (a) (red solid), (b) (blue dotted) and (c) (black dashed). Negative polarity indicates downwelling and positive velocity is upwelling. (e) radial flow flux as a function of distance from the slab center, normalized by slab stagnation half length. In all simulations, vertical mass exchange occurs in the vicinity of the slab.

be interesting to investigate stagnant slabs in different mantle viscosity structures, possibly including a thin layer above the 410 as predicted by the water-filter model (Bercovici & Karato, 2003; Karato, 2011).

6. Conclusions

The classic textbook anti-correlation between the 410-km and 660-km discontinuities is not a common feature in global subduction zones. While counter-initiative, major subduction zones where massive stagnant slabs have been imaged are characterized by strong positive correlations between the 410-km and 660-km discontinuity, with both discontinuities occurring at greater depths. Wavespeed and anisotropy models support vertical variations in thermal structure in the mid mantle. We interpret this circum-Pacific positive correlation as a result of cold, stagnant slab in the lower MTZ and an overall warmer return flows associated with the sinking of large, stagnant slabs into the lower mantle. This mode of mass exchange between the upper and lower mantle occurs in the close proximity of the (sinking) stagnant slabs. The global oceanic regions are associated with an overall thinner MTZ and a weak anti-correlation between the 410-km and

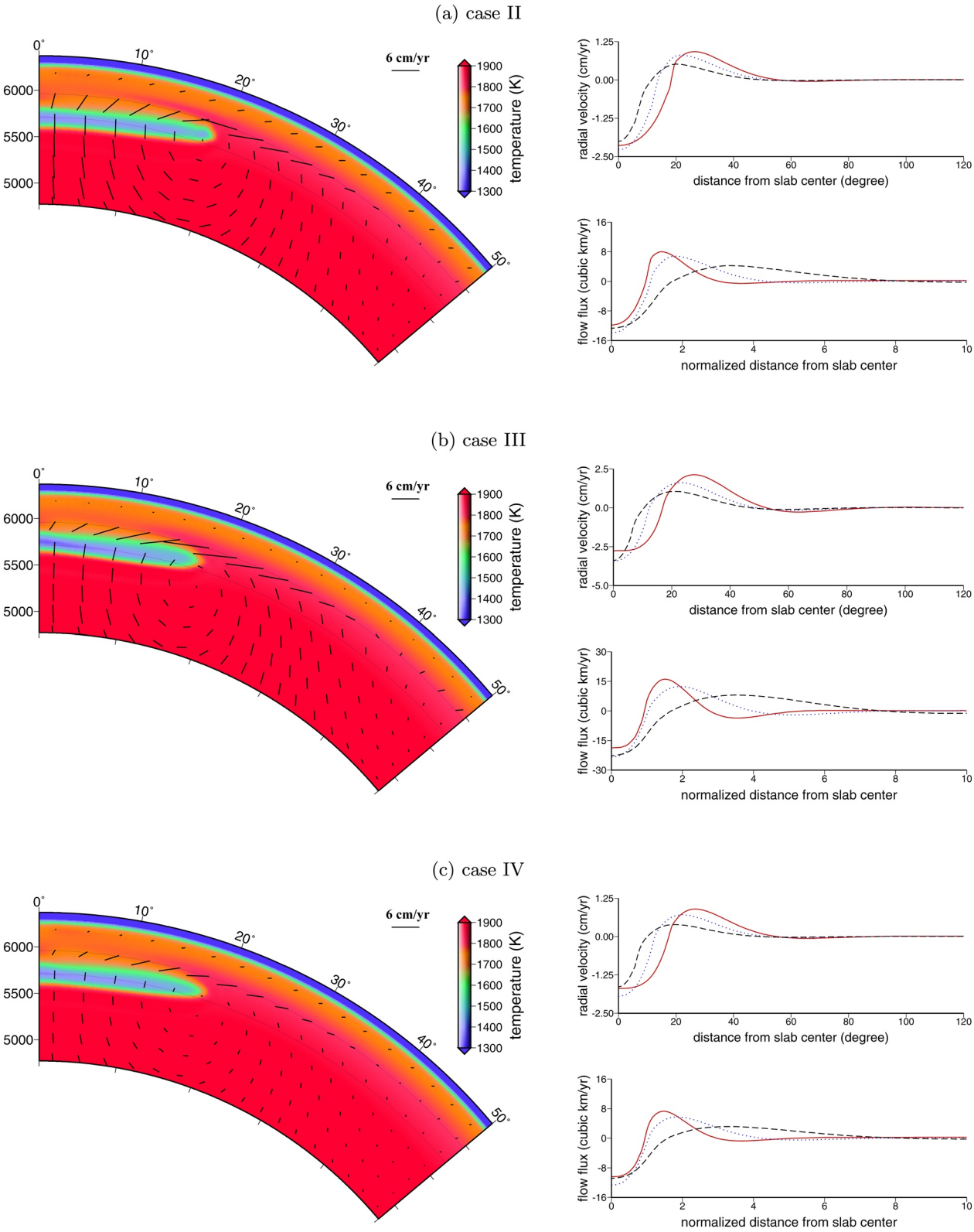

Figure 11. The same as Figure 10 but for different viscosity structures as shown in Figure 9.

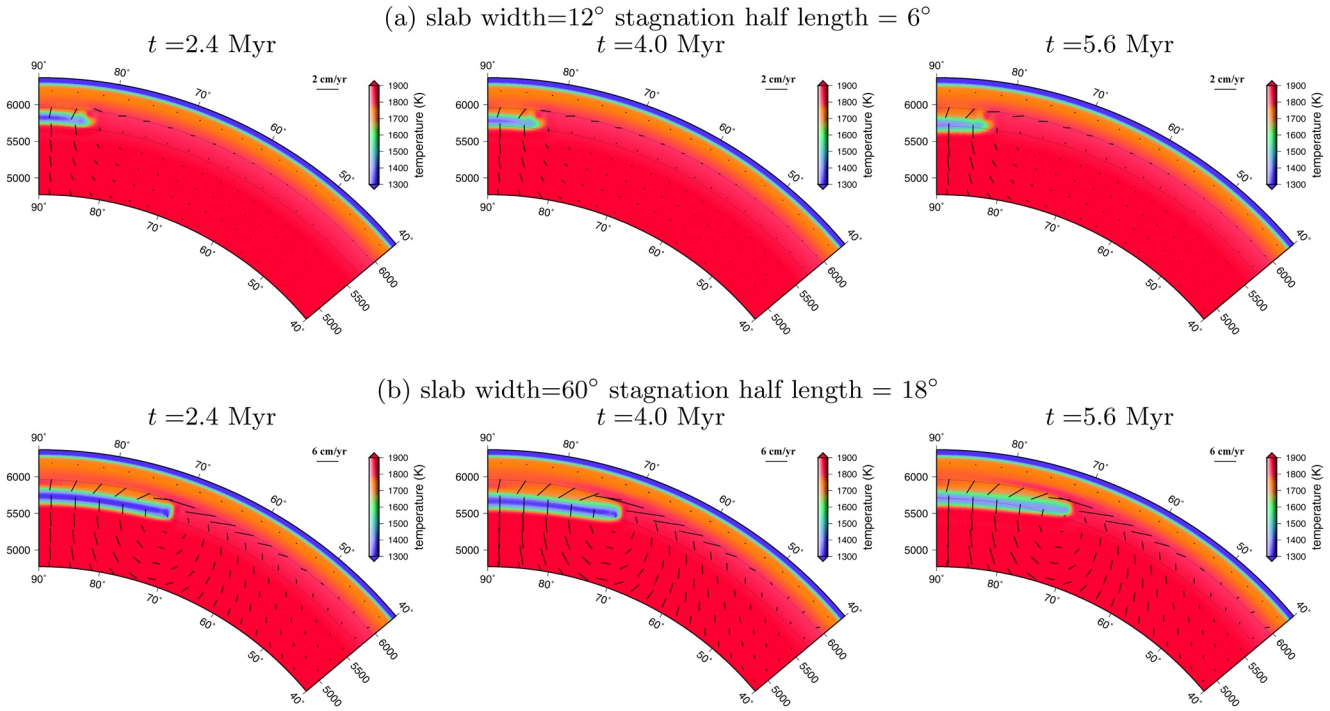

Figure 12. CitcomS simulations at different time steps t = 2.4, 4.0, and 5.6 Myr for (a) a small slab and (b) a large slab. Temperature and viscosity profiles are the same as in Figure 10. The simulation in (a) is the same as Figure 10c but with the width of the slab reduced to 12°. The simulation in (b) is identical to Figure 10a. The return flows become largely absent when width of the slab is significantly reduced.

660-km discontinuity depth perturbations, which indicates the existence of a weak return flow in the far-field oceanic mantle.

We have used a very simple model for stagnant slabs to investigate return flows associated with a large horizontal slab in the MTZ. Our simulations suggest that the strength of local return flows depends on the size of the slab, and, local return flows become largely absent when the width of the slab is significantly reduced. In the future, it would be worth investigating return flows in more realistic subduction scenarios. While we have used a constant super-adiabatic temperature gradient for the bulk mantle, the return flow model does not require temperature gradient to be constant but it may vary with depth. For example, mantle potential temperature could be higher in the lower mantle than in the upper mantle as the increased density due to phase transformations across the MTZ may overcome super-adiabatic thermal buoyancy.

Data Availability Statement

Seismic Data used in this research are available from the IRIS Data Management Center (http://www.iris.edu). CitcomS for mantle convection simulation is available at http://www.geodynamics.org/cig/software/citcoms/

Acknowledgments
The authors thank Dr. Maria Koroni, two anonymous reviewers and the Associated Editor for their constructive comments. The authors thank Editor Isabelle Manighetti for her professional handling of the manuscript. The authors thank Jeffrey Park and Mingming Li for their comments. This research was supported by the US National Science Foundation under Grants EAR-1737737 and EAR-2017218. The authors acknowledge Advanced Research Computing at Virginia Tech for providing computational resources and technical support.

References

Anderson, D. L. (1967). Phase changes in the upper mantle. *Science*, *157*, 1165–1173. https://doi.org/10.1126/science.157.3793.1165

Ballmer, M. D., Schmerr, N. C., Nakagawa, T., & Ritsema, J. (2015). Compositional mantle layering revealed by slab stagnation at ~1000-km depth. *Science.Advances*, *1*, e1500815. https://doi.org/10.1126/sciadv.1500815

Bercovici, D., & Karato, S. I. (2003). Whole-mantle convection and the transition-zone water filter. *Nature*, *425*, 39–44. https://doi.org/10.1038/nature01918

Bina, C. R., & Helffrich, G. (1994). Phase transition Clapeyron slopes and transition zone seismic discontinuity topography. *Journal of Geophysical Research*, *99*, 15853–15860. https://doi.org/10.1029/94jb00462

Birch, F. (1952). Elasticity and constitution of the Earth's interior. *Journal of Geophysical Research*, *57*, 227–286. https://doi.org/10.1029/jz057i002p00227

Chang, S.-J., Ferreira, A. M. G., Ritsema, J., van Heijst, H. J., & Woodhouse, J. H. (2014). Global radially anisotropic mantle structure from multiple datasets: A review, current challenges, and outlook. *Tectonophysics*, *617*, 1–19. https://doi.org/10.1016/j.tecto.2014.01.033

Christensen, U. (1995). Effects of phase transitions on mantle convection. *Annual Review of Earth and Planetary Sciences*, *23*, 65–87. https://doi.org/10.1146/annurev.ea.23.050195.000433

Christensen, U. R. (1996). The influence of trench migration on slab penetration into the lower mantle. *Earth and Planetary Science Letters*, *140*, 27–39. https://doi.org/10.1016/0012-821x(96)00023-4

Dahlen, F. A. (2005). Finite-frequency sensitivity kernels for boundary topography perturbations. *Geophysical Journal International*, *162*, 525–540. https://doi.org/10.1111/j.1365-246x.2005.02682.x

Deng, K., & Zhou, Y. (2015). Wave diffraction and resolution of mantle transition zone discontinuities in receiver function imaging. *Geophysical Journal International*, *201*, 2008–2025. https://doi.org/10.1093/gji/ggv124

Dokht, R. M. H., Gu, Y. J., & Sacchi, M. D. (2018). Migration imaging of the java subduction zones. *Journal of Geophysical Research: Solid Earth*, *123*, 1540–1558. https://doi.org/10.1002/2017jb014524

Dziewonski, A. M., & Anderson, D. L. (1981). Preliminary reference Earth model. *Physics of the Earth and Planetary Interiors*, *25*, 297–356. https://doi.org/10.1016/0031-9201(81)90046-7

Flanagan, M. P., & Shearer, P. M. (1998). Global mapping of topography on transition zone velocity discontinuities by stacking SS precursors. *Journal of Geophysical Research*, *103*, 2673–2692. https://doi.org/10.1029/97jb03212

Forsyth, D., & Uyeda, S. (1975). On the relative importance of the driving forces of plate motion. *Geophysical Journal International*, *43*, 163–200. https://doi.org/10.1111/j.1365-246x.1975.tb00631.x

Fukao, Y., & Obayashi, M. (2013). Subducted slabs stagnant above, penetrating through, and trapped below the 660 km discontinuity. *Journal of Geophysical Research: Solid Earth*, *118*, 5920–5938. https://doi.org/10.1002/2013jb010466

Gao, S. S., & Liu, K. H. (2014). Mantle transition zone discontinuities beneath the contiguous United States. *Journal of Geophysical Research: Solid Earth*, *119*, 6452–6468. https://doi.org/10.1002/2014jb011253

Gu, Y. J., Dziewoński, A. M., & Ekström, G. (2003). Simultaneous inversion for mantle shear velocity and topography of transition zone discontinuities. *Geophysical Journal International*, *154*, 559–583. https://doi.org/10.1046/j.1365-246x.2003.01967.x

Guo, Z., & Zhou, Y. (2020). Finite-frequency imaging of the global 410- and 660-km discontinuities using SS precursors. *Geophysical Journal International*, *220*, 1978–1994. https://doi.org/10.1093/gji/ggz546

Hafkenscheid, E., Wortel, M. J. R., & Spakman, W. (2006). Subduction history of the Tethyan region derived from seismic tomography and tectonic reconstructions. *Journal of Geophysical Research*, *111*, B08401. https://doi.org/10.1029/2005JB003791

Hager, B. H., & Richards, M. A. (1989). Long-wavelength variations in Earth's geoid: Physical models and dynamical implications. *Philosophical Transactions of the Royal Society A*, *328*, 309–327.

Hall, R. (2012). Late Jurassic-Cenozoic reconstructions of the Indonesian region and the Indian Ocean. *Tectonophysics*, *570–571*, 1–41. https://doi.org/10.1016/j.tecto.2012.04.021

Hall, R., & Spakman, W. (2015). Mantle structure and tectonic history of SE Asia. *Tectonophysics*, *658*, 14–45. https://doi.org/10.1016/j.tecto.2015.07.003

Heit, B., Yuan, X., Bianchi, M., Kind, R., & Gossler, J. (2010). Study of the lithospheric and upper-mantle discontinuities beneath eastern Asia by SS precursors. *Geophysical Journal International*, *183*, 252–266. https://doi.org/10.1111/j.1365-246x.2010.04714.x

Houser, C., Masters, G., Flanagan, M., & Shearer, P. (2008). Determination and analysis of long-wavelength transition zone structure using SS precursors. *Geophysical Journal International*, *174*, 178–194. https://doi.org/10.1111/j.1365-246x.2008.03719.x

Huang, Q., Schmerr, N., Waszek, L., & Beghein, C. (2019). Constraints on seismic anisotropy in the mantle transition zone from long-period SS precursors. *Journal of Geophysical Research: Solid Earth*, *124*, 6779–6800. https://doi.org/10.1029/2019jb017307

Karato, S.-i. (2011). Water distribution across the mantle transition zone and its implications for global material circulation. *Earth and Planetary Science Letters*, *301*, 413–423. https://doi.org/10.1016/j.epsl.2010.11.038

Katsura, T., & Ito, E. (1989). The system mg_2sio_4 -fe_2sio_4 at high pressures and temperatures; precise determination of stabilities of olivine, modified spinel, and spinel. *Journal of Geophysical Research*, *94*, 15663–16670. https://doi.org/10.1029/jb094ib11p15663

Kennett, B. L. N., & Engdahl, E. R. (1991). Traveltimes for global earthquake location and phase identification. *Geophysical Journal International*, *105*, 429–465. https://doi.org/10.1111/j.1365-246x.1991.tb06724.x

Khan, A., Connolly, J. A. D., & Olsen, N. (2006). Constraining the composition and thermal state of the mantle beneath Europe from inversion of long-period electromagnetic sounding data. *Journal of Geophysical Research*, *111*, B10102. https://doi.org/10.1029/2006JB004270

Koroni, M., Bozdağ, E., Paulssen, H., & Trampert, J. (2017). Sensitivity analysis of seismic waveforms to upper-mantle discontinuities using the adjoint method. *Geophysical Journal International*, *210*, 1965–1980. https://doi.org/10.1093/gji/ggx286

Koroni, M., Paulssen, H., & Trampert, J. (2019). Sensitivity kernels of pp precursor traveltimes and their limitations for imaging topography of discontinuities. *Geophysical Research Letters*, *46*, 698–707. https://doi.org/10.1029/2018gl081592

Koroni, M., & Trampert, J. (2016). The effect of topography of upper-mantle discontinuities on SS precursors. *Geophysical Journal International*, *204*, 667–681. https://doi.org/10.1093/gji/ggv471

Kushiro, I. (1986). Viscosity of partial melts in the upper mantle. *Journal of Geophysical Research*, *91*, 9343–9350. https://doi.org/10.1029/jb091ib09p09343

Laske, G., Masters, G., Ma, Z., & Pasyanos, M. (2013). Update on CRUST1.0-A 1-degree global model of Earth's crust. *EGU General Assembly Conference Abstracts*, *15*, 2658.

Lawrence, J. F., & Shearer, P. M. (2008). Imaging mantle transition zone thickness with SdS-SS finite-frequency sensitivity kernels. *Geophysical Journal International*, *174*, 143–158. https://doi.org/10.1111/j.1365-246x.2007.03673.x

Liu, K., & Zhou, Y. (2016). Travelling-wave green tensor and near-field Rayleigh-wave sensitivity. *Geophysical Journal International*, *205*, 134–145. https://doi.org/10.1093/gji/ggv564

Liu, X., & Zhong, S. (2016). The long-wavelength geoid from three-dimensional spherical models of thermal and thermochemical mantle convection. *Journal of Geophysical Research: Solid Earth*, *120*, 4572–4596. 10.1002/2015JB012016

Liu, Z., Park, J., & Karato, S. -I. (2016). Seismological detection of low-velocity anomalies surrounding the mantle transition zone in Japan subduction zone. *Geophysical Research Letters*, *43*, 2480–2487. https://doi.org/10.1002/2015gl067097

Liu, Z., Park, J., & Karato, S. -I. (2018). Seismic evidence for water transport out of the mantle transition zone beneath the European Alps. *Earth and Planetary Science Letters*, *482*, 93–104. https://doi.org/10.1016/j.epsl.2017.10.054

Mao, W., & Zhong, S. (2018). Slab stagnation due to a reduced viscosity layer beneath the mantle transition zone. *Nature Geoscience*, *11*, 876–881. https://doi.org/10.1038/s41561-018-0225-2

Moulik, P., & Ekström, G. (2014). An anisotropic shear velocity model of the Earth's mantle using normal modes, body waves, surface waves and long-period waveforms. *Geophysical Journal International*, *199*, 1713–1738. https://doi.org/10.1093/gji/ggu356

Nakagawa, T., & Buffett, B. A. (2010). Mass transport mechanism between the upper and lower mantle in numerical simulations of thermochemical mantle convection with multicomponent phase changes. *Earth and Planetary Science Letters*, *230*, 11–27.
Ringwood, A. E. (1969). Phase transformation in the mantle. *Earth and Planetary Science Letters*, *5*, 401–412.
Ringwood, A. E. (1994). Role of the transition zone and 660 km discontinuity in mantle dynamics. *Physics of the Earth and Planetary Interiors*, *86*, 5–24. https://doi.org/10.1016/0031-9201(94)05058-9
Ritsema, J., Deuss, A., van Heijst, H. J., & Woodhouse, J. H. (2011). S40RTS: A degree-40 shear-velocity model for the mantle from new Rayleigh wave dispersion, teleseismic traveltime and normal-mode splitting function measurements. *Geophysical Journal International*, *184*, 1223–1236. https://doi.org/10.1111/j.1365-246x.2010.04884.x
Sandwell, D. T., & Renkin, M. L. (1988). Compensation of swells and plateaus in the North Pacific: No direct evidence for mantle convection. *Journal of Geophysical Research*, *93*, 2775–2783. https://doi.org/10.1029/jb093ib04p02775
Schaeffer, A. J., & Lebedev, S. (2013). Global shear speed structure of the upper mantle and transition zone. *Geophysical Journal International*, *194*, 417–449. https://doi.org/10.1093/gji/ggt095
Schmerr, N., & Garnero, E. (2006). Investigation of upper mantle discontinuity structure beneath the central Pacific using SS precursors. *Journal of Geophysical Research*, *111*, B08305. https://doi.org/10.1029/2005JB004197
Schmerr, N., & Garnero, E. J. (2007). Upper mantle discontinuity topography from thermal and chemical heterogeneity. *Science*, *318*, 623–626. https://doi.org/10.1126/science.1145962
Seno, T., & Maruyama, S. (1984). Paleogeographic reconstruction and origin of the Philippine Sea. *Tectonophysics*, *102*, 53–84. https://doi.org/10.1016/0040-1951(84)90008-8
Shearer, P. M. (1991). Constraints on upper mantle discontinuities from observations of long-period reflected and converted phases. *Journal of Geophysical Research*, *96*, 18147–18182. https://doi.org/10.1029/91jb01592
Shen, X., Zhou, H., & Kawakatsu, H. (2008). Mapping the upper mantle discontinuities beneath china with teleseismic receiver functions. *Earth Planets and Space*, *60*, 713–719. https://doi.org/10.1186/bf03352819
Sigloch, K., McQuarrie, N., & Nolet, G. (2008). Two-stage subduction history under North America inferred from multiple-frequency tomography. *Nature Geoscience*, *1*, 458–462. https://doi.org/10.1038/ngeo231
Smyth, J. R., & Jacobsen, S. D. (2006). Nominally anhydrous minerals and Earth's deep water cycle. *Earth's Deep Water Cycle*, *1*, 1–11.
Sturgeon, W., Ferreira, A. M. G., Faccenda, M., Chang, S. J., & Schardong, L. (2019). On the origin of radial anisotropy near subducted slabs in the midmantle. *Geochemistry, Geophysics, Geosystems*, *20*, 5105–5125. https://doi.org/10.1029/2019gc008462
Tan, E., Choi, E., Thoutireddy, P., Gurnis, M., & Aivazis, M. (2006). Geoframework: Coupling multiple models of mantle convection within a computational framework. *Geochemistry, Geophysics, Geosystems*, *7*, Q06001. https://doi.org/10.1029/2005GC001155
Tao, K., Grand, S. P., & Niu, F. (2018). Seismic structure of the upper mantle beneath eastern Asia from full waveform seismic tomography. *Geochemistry, Geophysics, Geosystems*, *19*, 2732–2763. https://doi.org/10.1029/2018gc007460
Tauzin, B., Debayle, E., & Wittlinger, G. (2010). Seismic evidence for a global low-velocity layer within the Earth's upper mantle. *Nature Geoscience*, *3*, 718–721. https://doi.org/10.1038/NGEO969
Tian, Y., Zhou, Y., Sigloch, K., Nolet, G., & Laske, G. (2011). Structure of North American mantle constrained by simultaneous inversion of multiple-frequency SH,SS, and love waves. *Journal of Geophysical Research*, *116*, B02307. https://doi.org/10.1029/2010JB007704
Till, C. B., Elkins-Tanton, L. T., & Fischer, K. M. (2010). A mechanism for low-extent melts at the lithosphere-asthenosphere boundary. *Geochemistry, Geophysics, Geosystems*, *11*, Q10015. https://doi.org/10.1029/2010GC003234
Toffelmier, D. A., & Tyburczy, J. A. (2007). Electromagnetic detection of a 410-km-deep melt layer in the southwestern United States. *Nature*, *447*, 991–994. https://doi.org/10.1038/nature05922
Turcotte, D. L., & Schubert, G. (2002). *Geodynamics* (second edition.). Cambridge University Press.
Vallier, T. L., Windom, K. E., Seifert, K. E., & Thiede, J. (1980). Volcanic rocks cored on Hess rise, western Pacific Ocean. *Nature*, *286*, 48–50. https://doi.org/10.1038/286048a0
van der Hilst, R. D., Widiyantoro, S., & Engdahl, E. R. (1997). Evidence for deep mantle circulation from global tomography. *Nature*, *386*, 578–584. https://doi.org/10.1038/386578a0
van Keken, P., & Zhong, S. (1999). Mixing in a 3-D spherical model of present-day mantle convection. *Earth and Planetary Science Letters*, *171*, 533–547. https://doi.org/10.1016/s0012-821x(99)00181-8
Verhoeven, O., Mocquet, A., Vacher, P., Rivoldini, A., Menvielle, M., Arrial, P.-A., et al. (2009). Constraints on thermal state and composition of the Earth's lower mantle from electromagnetic impedances and seismic data. *Journal of Geophysical Research*, *114*, B03302. https://doi.org/10.1029/2008JB005678
Wada, I., & King, S. (2015). Dynamics of subducting slabs: Numerical modeling and constraints from seismology, geoid, topography, geochemistry, and petrology. *Treatise on Geophysics*, *7*, 339–391. https://doi.org/10.1016/b978-0-444-53802-4.00132-9
Wang, Y., & Pavlis, G. L. (2016). Roughness of the mantle transition zone discontinuities revealed by high-resolution wavefield imaging. *Journal of Geophysical Research: Solid Earth*, *121*, 6757. https://doi.org/10.1002/2016JB013205
Waszek, L., Schmerr, N. C., & Ballmer, M. D. (2018). Global observations of reflectors in the mid-mantle with implications for mantle structure and dynamics. *Nature Communications*, *9*, 385. https://doi.org/10.1038/s41467-017-02709-4
Webb, S. C., & Forsyth, D. W. (1998). Structure of the upper mantle under the EPR from waveform inversion of regional events. *Nature*, *280*, 1227–1229. https://doi.org/10.1126/science.280.5367.1227
Weidner, D. J., & Wang, Y. (2000). Phase transformations: Implications for mantle structure. *Earth's Deep Interior: Mineral Physics and Tomography From the Atomic to the Global Scale*, *117*, 215–235. https://doi.org/10.1029/gm117p0215
Wessel, P., Bercovici, D., & Kroenke, L. W. (1994). The possible reflection of mantle discontinuities in Pacific geoid and bathymetry. *Geophysical Research Letters*, *21*, 1943–1946. https://doi.org/10.1029/94gl01815
Xu, W., Lithgow-Bertelloni, C., Stixrude, L., & Ritsema, J. (2008). The effect of bulk composition and temperature on mantle seismic structure. *Earth and Planetary Science Letters*, *275*, 70–79. https://doi.org/10.1016/j.epsl.2008.08.012
Xue, J., & King, S. D. (2016). Geodynamic investigation of a cretaceous superplume in the Pacific Ocean. *Physics of the Earth and Planetary Interiors*, *257*, 137–148. https://doi.org/10.1016/j.pepi.2016.05.018
Yu, C., Day, E. A., de Hoop, M. V., Campillo, M., & van der Hilst, R. D. (2017). Mapping mantle transition zone discontinuities beneath the central pacific with array processing of SS precursors. *Journal of Geophysical Research: Solid Earth*, *122*, 10364–10378. https://doi.org/10.1002/2017jb014327
Zhong, S., McNamara, A., Tan, E., Moresi, L., & Gurnis, M. (2008). A benchmark study on mantle convection in a 3-D spherical shell using CitcomS. *Geochemistry, Geophysics, Geosystems*, *9*, Q10017. https://doi.org/10.1029/2008gc002048
Zhong, S., Zuber, M. T., Moresi, L., & Gurnis, M. (2000). Role of temperature-dependent viscosity and surface plates in spherical shell models of mantle convection. *Journal of Geophysical Research*, *105*, 11063–11082. https://doi.org/10.1029/2000jb900003

Zhou, Q., Liu, L., & Hu, J. (2018). Western US volcanism due to intruding oceanic mantle driven by ancient Farallon slabs. *Nature Geoscience*, *11*, 70–76. https://doi.org/10.1038/s41561-017-0035-y

Zhou, Y. (2009). Multimode surface wave sensitivity kernels in radially anisotropic Earth media. *Geophysical Journal International*, *176*, 865–888. https://doi.org/10.1111/j.1365-246x.2008.04010.x

Zhou, Y. (2018). Anomalous mantle transition zone beneath the Yellowstone hotspot track. *Nature Geoscience*, *11*, 449–453. https://doi.org/10.1038/s41561-018-0126-4

Zhu, H., Komatitsch, D., & Tromp, J. (2017). Radial anisotropy of the North American upper mantle based on adjoint tomography with USArray. *Geophysical Journal International*, *211*, 349–377. https://doi.org/10.1093/gji/ggx305